Clothing spiny nanoprobes against the mononuclear phagocyte system clearance *in vivo*: Photoacoustic diagnosis and photothermal treatment of early stage liver cancer with erythrocyte membrane-camouflaged gold nanostars

Xiazi Huang [a,b,c,1], Wenting Shang [b,c,1], Han Deng [b,d], Yingying Zhou [a], Fei Cao [a], Chihua Fang [d], Puxiang Lai [a,*], Jie Tian [b,c,**]

[a] Department of Biomedical Engineering, The Hong Kong Polytechnic University, Hong Kong SAR, China
[b] CAS Key Laboratory of Molecular Imaging, Institute of Automation, Chinese Academy of Sciences, Beijing, China
[c] Beijing Advanced Innovation Center for Big Data-Based Precision Medicine, School of Medicine, Beihang University, Beijing, China
[d] Department of Hepatobiliary Surgery, Zhujiang Hospital, Southern Medical University, Guangzhou, China

ARTICLE INFO

ABSTRACT

Nanoprobes have been increasingly applied in photoacoustic imaging to improve the diagnosis and treatment of diseases, especially the liver cancer, the fourth leading cause of cancer-related deaths worldwide. The mononuclear phagocytic system (MPS), however, exhibits a crucial impediment to the probe usage, preventing the accumulation of probes within the liver. This, in turn, paralyzes the effort of diagnosis enhancement. To overcome the MPS clearance, a biomimetic probe consisting of erythrocyte membrane-camouflaged gold nanostars was designed and synthesized in this study. The probe possesses broad absorption spectrum, photostability, and photothermal conversion efficiency. More importantly, it yields preeminent immune escape ability, thus being able to escape the MPS clearance and greatly boost the accumulation of probes at the tumor sites with prolonged blood circulation. Experimentally, we demonstrate that the probe can serve as an effective nanoprobe to enhance the *in vivo* photoacoustic imaging and photothermal treatment of *in situ* early stage liver tumors in mice.

1. Introduction

Photoacoustic imaging (PAI) is a noninvasive hybrid modality that is able to reveal high optical contrast at ultrasonic resolution in relatively thick soft tissue, like liver, by converting nonionizing optical radiation into not-so-scattered ultrasonic waves [1–4]. PAI has many advantages, such as safety, high resolution, high specificity, and relatively low cost when compared with traditional imaging modalities such as X-ray computed tomography, nuclear magnetic imaging, and magnetic resonance imaging. More importantly, many endogenous tissue chromophores (optical absorbers), such as oxy-/deoxy-hemoglobin, melanin, and water, can provide rich structural and functional information [5]. Therefore, this technology is intrinsically promising for precise detection of tissue heterogeneities, such as cancer [6]. However, the photon flux, and hence the PA signal strength attenuates very rapidly with penetration depth. Moreover, for deep organs, especially the liver, the background (normal tissue) poses strong optical absorption and scattering over visible optical spectrum, severely impairing the diagnosis of the liver cancer [7], the fourth leading cause of cancer-related deaths worldwide [8]. In this scenario, exogenous agents with excellent near-infrared (NIR) absorption are of great significance: the NIR light yields deeper penetration depth [9,10].

Among the many exogenous agents, plasmonic noble metal nanoparticles have seen extensive exploitation in PAI; due to surface plasmon resonance, the optical absorption of these nanoparticles can be a few orders of magnitude larger than that of traditional contrast agents such as dyes [11]. Gold nanostar (AuNS) is such a representative owing to its favorable and tunable absorption spectrum in the NIR region [12–14]. Furthermore, the sharp branches of the AuNS can act as 'lightning antennas', strongly enhancing the onsite optical absorption [15]. Such tunable increase in absorption can benefit not only PAI on diagnosis, but also photothermal therapy (PTT), a technique that has gained great attention in recent years with a goal of treating primary tumors and preventing metastatic cancer [16,17]. The mechanism of PTT is similar to that mediating the photoacoustic effect, *i.e.*, through

---

* Corresponding author at: Department of Biomedical Engineering, The Hong Kong Polytechnic University, Hong Kong SAR, China.
** Corresponding author at: CAS Key Laboratory of Molecular Imaging, Institute of Automation, Chinese Academy of Sciences, Beijing, China.
E-mail addresses: puxiang.lai@polyu.edu.hk (P. Lai), jie.tian@ia.ac.cn (J. Tian).
[1] These authors contributed equally to this work.

tissue absorption, whereby light is converted into thermal energy after its adequate accumulation within tumors [18]. Consequently, AuNS represents an attractive choice of exogenous probe to detect (*via* PAI) and treat (*via* PTT) early stage liver cancers. With optically absorbing AuNSs as microscopic heat sources, the therapeutic accuracy of PTT can be considerably improved while injury to the surrounding normal tissues can be minimized.

It must be pointed out, however, mononuclear phagocytic systems (MPS) populate richly in organs like liver and spleen with a key function to filter out toxins and foreign invaders in the blood [19]. This action, however, also prevents AuNS from reaching and accumulating at the target diseased site(s) [20], posing a major challenge of early liver cancer diagnosis: how to ensure an effective yet controllable accumulation of nanoprobes at the hepatic tumor. In the meanwhile, since nanoparticles have 10^2-10^3 times greater probability of being sequestrated in the liver sinusoid than in the extra-hepatic circulation [20], the whole liver is "lightened" photoacoustically, resulting in a low signal-to-noise ratio (SNR) of liver tumor detection. Therefore, it is imperative to design novel nanoparticle materials or structures to overcome the MPS clearance and effectively accumulate at hepatic tumor(s).

To address this challenge, researchers have designed biologically natural or biomimetic nanostructures [21,22], such as native substances (*e.g.*, cells, viruses, bacteria) with intrinsic properties of regulated diversity (*e.g.*, growth, metabolism, immunity) that allow them to escape the MPS [23,24]. The red blood cell membrane (RBCm) is one such promising option for *in vivo* liver applications due to its many advantages, including immune escape ability and prolonged blood circulation [25,26]. Furthermore, "self-markers" on the surface of the RBCm, such as CD47 proteins, acidic sialyl moieties, and glycans, can be easily encoded to entrust nanoparticles coated by the membrane with special biofunctions [27]. Therefore, RBCm-camouflaged nanoparticles have great potentials in cancer applications, such as photothermal-chemotherapeutic synergistic treatment [28], photodynamic therapy [29], pro-drug delivery systems [30], and starvation therapy [31]. At the cellular level, nanoparticles camouflaged by the erythrocyte membrane have been confirmed to exhibit immune escape and slower blood clearance [32,33]. Benefits of reduced MPS clearance and prolonged blood circulation *in vivo* are obvious: a greater amount of probe can accumulate at the tumor site(s) and produce much stronger PA signals from the region of interest, resulting in improved diagnostic and therapeutic outcomes.

To this end, we have designed and assembled a novel RBC membrane-coated AuNS probe (RBCm-AuNS) in this study. AuNSs with desired NIR absorption characteristics are enveloped with RBC membranes, which successfully eludes the MPS clearance and, at the same time, substantially enhances the accumulation of nanoprobes in the hepatocellular carcinoma model with prolonged circulation time. Such a clothed probe provides an effective and accurate model for the diagnosis and treatment of early stage liver cancer, as demonstrated experimentally. Three *in situ* tumors of mouse's liver smaller than 2 mm in diameter can be identified with PAI, and treatment with PTT can significantly reduce the tumor size and double the survival time of affected mice. Collectively, RBCm-AuNSs can potentially serve as a promising nanoprobe to improve the optical diagnosis and treatment of small liver tumors *in vivo*.

2. Methods

2.1. Synthesis and characterization of RBCm-AuNSs

RBC membrane-derived vesicles were prepared as described previously [34] with a few modifications. Briefly, whole blood (~2 mL) was collected from Kunming mice (males, 38–40 g) using a syringe that lightly pierced the submaxillary venous plexus. The blood was suspended in 10 mL erythrocyte preserving fluid and centrifuged at 3000 rpm for 5 min at 4 °C to collect RBCs. RBCs were washed three times with ice cold $1 \times$ PBS containing 1 mM EDTA-2Na, suspended in excess 0.25 mM EDTA-2Na in an ice bath for 12 h to allow for hemolysis to occur, and then collected again by centrifugation at 10,000 rpm for 15 min to remove serum and buffy coat. Following three washes with cold hypotonic solution, the collected RBC membranes were sonicated in a capped glass bottle for 10 min using a bath sonicator (Fisher Scientific, Waltham, MA, USA) set at 42 kHz and a power of 100 W. The resultant vesicles were subsequently extruded in sequence through 1000-nm, 400-nm, 200-nm, and 100-nm polycarbonate porous membranes using an Avanti mini extruder (Avanti Polar Lipids, Alabaster, AL, USA).

AuNSs were prepared using a seed-mediated growth method [35]. The gold seeds were firstly synthesized by adding trisodium citrate (6 mL, 1%) into a $HAuCl_4$ solution (40 mL, 1 mM) with heating (95 °C) and stirring (500 rpm). After 5 min, a zinzolin gold seed solution was obtained, and heating and stirring were stopped to let the solution cool down to room temperature. Subsequently, $HAuCl_4$ (50 mL, 1 mM), HCl (0.2 mL, 1 M), and double-deionized water (150 mL) were mixed and stirred at 500 rpm. A 2-mL aliquot of the gold seed solution was added to the mixture and let stand for 1 min. After that, $AgNO_3$ (2 mL, 2 mM) and ascorbic acid (2 mL, 0.1 mM) were added simultaneously to generate the AuNS solution. The original AuNS solution was stored in the refrigerator at 4 °C until use, following prior centrifugation at 6500 rpm for 10 min.

To synthesize the final RBCm-AuNSs, we mixed the prepared RBC membrane-derived vesicles and AuNS solution at a 1:1 surface area ratio (S_{RBCm}/S_{AuNSs}), following the surface area analysis (Supplementary material). The mixtures were extruded sequentially through 400-nm and 200-nm polycarbonate porous membranes using an Avanti mini extruder. Afterwards, the mixtures were centrifuged at 10,000 rpm for 10 min to remove the excessive free RBC membrane vesicles and were washed three times with deionized water. The resultant RBCm-AuNSs were then re-dispersed for further transmission electron microscopy (TEM), DLS, zeta potential, and ultraviolet-visible (UV-VIS) characterizations.

2.2. RBCm-AuNS characterization

The morphology of AuNSs and RBCm-AuNSs were characterized by TEM using a JEOL-1011 microscope (JEOL, Tokyo, Japan) with a 100-kV acceleration voltage. Zeta potential and size were analyzed with a ZEM 3600 Malvern Zetasizer (Malvern, UK). Optical absorption spectra were monitored using a UV-VIS-NIR spectrophotometer (Shimadzu, Kyoto, Japan). Sodium dodecyl sulfate-polyacrylamine gel electrophoresis (SDS-PAGE) was utilized to characterize membrane proteins.

2.3. Stability test of RBCm-AuNSs

The stability of RBCm-AuNSs were tested with the UV-VIS-NIR spectrophotometer by monitoring the change in optical absorption spectra. To this end, 100 μg/mL RBCm-AuNSs were dissolved in 5 mL FBS and stored at room temperature. Optical absorption spectra were recorded every 12 h.

2.4. Photothermal performance assay

Continuous 785-nm NIR laser illumination with a spot size of 4–5 mm was used to test the photothermal effect. The power density was 2 W/cm². The distance between laser source output and sample was set at 1 cm. Before irradiation, samples were dissolved in deionized water to achieve an RBCm-AuNSs concentration of 0, 20, 60, and 100 μg/mL, respectively. Then, 200 mL of

each sample were used for photothermal measurements. Temperature variations of all samples were acquired using a FLUKE Ti25 infrared thermal imaging camera (Everett, WA, USA) at 50 s intervals, with an accuracy of 0.1 °C. For optical stability detection, 60 and 100 μg/mL RBCm-AuNSs solutions were analyzed at 5-min intervals by fits and starts using the same laser conditions stated above. All experiments were conducted in triplicate.

2.5. Cell culture

Hep-G2 and HUH-7 cells were cultured separately in DMEM supplemented with 10% (v/v) FBS and 1% penicillin-streptomycin solution, under a 5% CO_2 atmosphere and 37 °C. RAW264.7 cells were cultured in DMEM supplemented with 10% (v/v) FBS and 1% penicillin-streptomycin solution, under a 5% CO_2 atmosphere and 37 °C.

2.6. Cytotoxicity assay

The cytotoxicity of probes was tested on Hep-G2 and HUH-7 cells. Cells were seeded at a density of 1×10^4/well in 96-well cell culture plates and incubated at 37 °C under a 5% CO_2 atmosphere for 24 h. Then, cells were treated with various concentrations (0, 20, 60, 100, 140, 180, and 220 μg/mL) of RBCm-AuNSs (100 μL/well) for 24 h. Finally, 100 μL/well of CCK-8/culture medium (10 μL/100 μL) was supplemented in each well and the plates were incubated for an additional 3 h under the same conditions. A Synergy HT microplate reader (BioTek, Winooski, VT, USA) was used to measure the absorbance of each well at 450 nm (OD 450). The following formula was used to calculate cell viability: Cell Viability (%) = [(As-Ab)/(Ac- Ab)] × 100%, where As, Ac, and Ab represent the OD 450 of treatment group, control group, and blank, respectively.

2.7. In vitro PTT assay

We used calcein-AM and propidium iodide (PI) staining to visually test the photothermal effect of RBCm-AuNSs. Hep-G2 cells were seeded in 6-well plates at 37 °C under 5% CO_2 atmosphere for 24 h. The original medium was washed off, followed by the addition of medium containing 60 μg/mL or 100 μg/mL RBCm-AuNSs, whereas medium without nanotubes was used as a control. After 4 h of continuous incubation, the cells were exposed to 785-nm laser illumination (1 W/cm^2) for 5 min in an already outlined area. Subsequently, the cells were washed gently twice with 1× Assay buffer, after which calcein-AM and PI were added. The cells were incubated for another 15 min and visualized by an inverted Leica M205 FA fluorescence microscope (Leica, Jena, Germany).

For quantitative analysis, Hep-G2 cells were cultured at a density of 1×10^4/well in a 96-well plate at 37 °C under a 5% CO_2 atmosphere for 24 h. Then, cells were randomly divided into four groups: control group, RBCm-AuNSs group, laser group, and RBCm-AuNSs with laser group. In the control group, cells were replaced with new routine culture medium as stated before. In the RBCm-AuNSs group and RBCm-AuNSs with laser group, cells were treated with various concentrations (10, 20, 40, 60, 80, and 100 μg/mL) of RBCm-AuNSs for 4 h. After that, cells in the RBCm-AuNSs with laser group were washed three times with PBS and then irradiated with a 785-nm laser under 2 W/cm^2 for 3 min. The same laser treatment procedure was applied also to the laser group but in the absence of RBCm-AuNSs. Afterwards, CCK-8 was used as discussed earlier.

2.8. Intracellular uptake assay

RAW264.7 cells were cultured to 70% confluence in a 10-mm dish at 37 °C under a 5% CO_2 atmosphere, and were then incubated with DMEM containing 100 μg/mL RBCm-AuNSs for another 6 h. Following the incubation, DMEM was poured off from the dish without any rinsing, the cells were immediately covered with electron microscope fixative, and collected into a centrifuge tube by scraping them gently off the dish. After further addition of electron microscope fixative, the cells were fixed for 2 h at room temperature and then transferred to a 4 °C refrigerator to be ready for subsequent experiments.

2.9. Biodistribution studies

For biodistribution studies, RBCm-AuNSs were first embedded with Cy7-NS for fluorescent imaging through a small animal optical molecular in vivo imaging system (IVIS Spectrum; PerkinElmer, Waltham, MA, USA) assembled with an appropriate optical filter. RBCm-AuNSs and Cy7-NS were mixed at an 8:1 M ratio and shaken overnight. Then, the mixture was centrifuged at 10,000 rpm for 10 min, and the pellet was washed three times with dimethyl sulfoxide/PBS (v/v, 1:99) to remove any free Cy7-NS. Liver tumor-bearing mice were prepared by injecting 1×10^6 Hep-G2 cells into the livers of 3 mice. After 2 weeks-breeding, the mice were injected with 200 μL RBCm-AuNSs-Cy7 (2 mg/mL). Pilot pictures were taken using the IVIS before and 1, 3, 6, 8, 10, 12, 24, 36, 48, 60, 72 h after the injection to monitor the biodistribution of RBCm-AuNSs in vivo. After 72 h, the mice were necropsied; their organs and tumors were then used to study metabolic pathways by way of fluorescence intensity measurements. All animal procedures were carried out in accordance with the guidelines approved by the Animal Ethics Committee of the Chinese Academy of Sciences.

2.10. In vitro and in vivo PAI

For in vitro PAI, various concentrations (0, 20, 40, 60, 100, 150, and 200 μg/mL) of RBCm-AuNSs dispersions were filled into cylindrical phantoms made of agarose, which were then positioned in a Multispectral Optoacoustic Tomography (MSOT) system (iTheraMedical, Munich, Germany). The MSOT system contains an optical parametric oscillator laser with tunable wavelength to provide excitation for the PA effect. An arc transducer aligned with the laser detects the PA signals from the subject. ViewMSOT software was utilized to process the PA images after acquisition. For quantitative analysis, regions of interest were drawn over the sample, and their averaged PA intensity values were recorded and calculated.

For in vivo PA imaging, six male nude mice (BALB/c, 17–19 g, 5 weeks) were injected separately with 1×10^6 Hep-G2 cells into the liver and then bred for 2 weeks. These mice were randomly divided into two groups. After anesthetization with 5% isoflurane, the mice were positioned in the MSOT system to acquire PA images at the liver section; this group of mice constituted the control group. Additional PA images at the same position were recorded at 1, 3, 6, 8, 12, 24, 36, 48, 60, and 72 h, after the mice received 200 μL of RBCm-AuNSs (2 mg/mL) intravenously. And the other group were treated with the same amount of AuNSs. PA signals from the AuNSs and RBCm-AuNSs were extracted using the unmixing spectra module of the imaging system to exclude signal contributions from oxy-/deoxy-hemoglobin in vivo. All mice were dissected at 72 h after imaging, with tumors being harvested, fixed with 4% paraformaldehyde, sectioned into slices, and stained with hematoxylin and eosin (H&E) for histological analysis.

2.11. In vivo PTT efficacy

Twenty-four liver tumor-bearing mice were prepared as described earlier. When tumor volume reached about 10 mm^3, mice were randomly divided into four evenly numbered groups: control group, RBCm-AuNSs group, laser group, and RBCm-AuNSs with laser group. In the control group, healthy mice did not receive
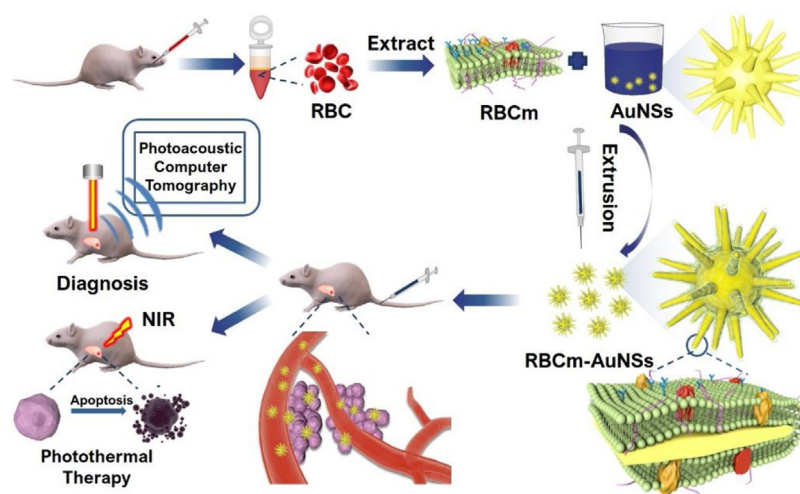
Scheme 1. Schematic illustration of RBCm-AuNSs for enhanced liver cancer photoacoustic diagnosis and photothermal therapy.

any treatment. In the laser group, tumor-bearing mice were irradiated with a 785-nm laser ($2\,W/cm^2$) for 5 min. In the other two groups, tumor-bearing mice received $200\,\mu L$ of RBCm-AuNSs ($2\,mg/mL$) intravenously, but only mice in the RBCm-AuNSs with laser group were also irradiated with a 785-nm laser ($2\,W/cm^2$) for 5 min at 48 h post-injection. The temperature elevation of tumors was recorded during the photothermal treatment using an infrared thermal imaging camera. Body weight of each mouse from all groups was measured every other day. The mice were dissected after death, with tumors and major organs including the heart, liver, spleen, lung, and kidney being harvested, fixed with 4% paraformaldehyde, sectioned into slices, and stained with H&E for histological analysis.

2.12. Statistical analyses

GraphPad Prism 5 software (GraphPad Software, San Diego, CA, USA) was used for statistical analysis. A *t*-test was used to determine differences among different groups. **p < 0.001 and ***p < 0.0001 were considered statistically significant, whereas n.s. indicated no significant difference between the selected two groups.

3. Results

3.1. Synthesis and characteristics of RBCm-AuNSs

We successfully synthesized RBCm-AuNSs which have broad absorption spectrum and bio-protein characterization through the route illustrated in Scheme 1. Briefly, RBCm-AuNSs were prepared following two successive steps. First, AuNSs were synthesized by the seed-mediated growth method and appeared a blue-black color (Fig. S1A) [35]. Then, the mixture containing RBC membranes and AuNSs were extruded through an Avanti mini extruder. The color of RBCm-AuNSs did not differ much from that of AuNSs (Fig. S1B). The as-prepared AuNSs and RBCm-AuNSs were observed by TEM (Fig. 1A and B). Semi-transparent membranes of less than 10 nm in thickness appeared tightly wrapped around the AuNS surface in a vacuum (Fig. 1B). The hydrodynamic size of AuNS and RBCm-AuNS were tested by DLS and are shown in Fig. 1C. The average diameter of RBCm-AuNS increased slightly from 103.6 nm (corresponding to that of AuNSs alone) to 125.4 nm. Such increase of 21.8 nm in diameter was attributed to the RBCm containing the lipid bilayer. The clothing process also shifted the zeta potential of AuNS from approximately -11.47 mV to -13.10 mV, the latter cor-

responding closely to the zeta potential of RBC membrane (Table S1). Results from the TEM, DLS, and zeta potential measurements prove that RBC membranes successfully clothe the spiny AuNSs, and hence the as-prepared RBCm-AuNSs support their use for further experiments.

Following the camouflage, complex membrane proteins on the surface of RBCm-AuNSs were examined by SDS-PAGE. Empty RBC membranes and AuNSs were employed as parallel controls. As shown in Fig. 1D, empty RBC membrane and RBCm-AuNSs shared the same protein bands, whereas no bands were detected in the AuNSs lane, indicating that membrane proteins were preserved during the preparation of RBCm-AuNSs. The spectral absorption characteristic of RBCm-AuNS is also an important index for optical diagnosis and treatment. So, we measured the UV-VIS absorption spectrum of RBCm-AuNSs. It exhibited a broad and strong absorption in the NIR region from 600 to 1000 nm (Fig. 1E), making it promising for both photoacoustic and photothermal effects. It is worth noted that the characteristic absorption peaks of RBCm-AuNSs can be distinguished from that of deoxyhemoglobin (Hb) and oxyhemoglobin (HbO_2). This allows for reliable extraction of signals contributed by the probes from the blood background during *in vivo* imaging. These results suggest that we have successfully synthesized RBCm-AuNSs, which retain the original structural features of both AuNSs and RBC membranes.

3.2. The photoacoustic property of RBCm-AuNSs in vitro

Due to the strong absorption of RBCm-AuNSs from 600 to 950 nm, the as-prepared probes were expected to produce strong PA emissions. To assess that, phantom samples with different probe concentrations were tested using the MSOT system. As seen, the brightness increases with the probe concentration (Fig. 2A). Actually, the PA signal strength, as measured by the pixel intensity, reveals an upward trend and a linear relationship with the concentration of RBCm-AuNSs ($R^2 = 0.9922$) of the sample (Fig. 2B). Therefore, the accumulation of the as-prepared probes allows us to better image the target site(s) photoacoustically. Note that. However, excessive probe concentration may result in osmosis that may affect the viability and activity of normal cells.

3.3. Stability, cytotoxicity evaluation and intracellular uptake of RBCm-AuNSs

In order to prove the beneficial properties of RBCm-AuNSs *in vivo*, their stability in FBS were examined. Even after sus-
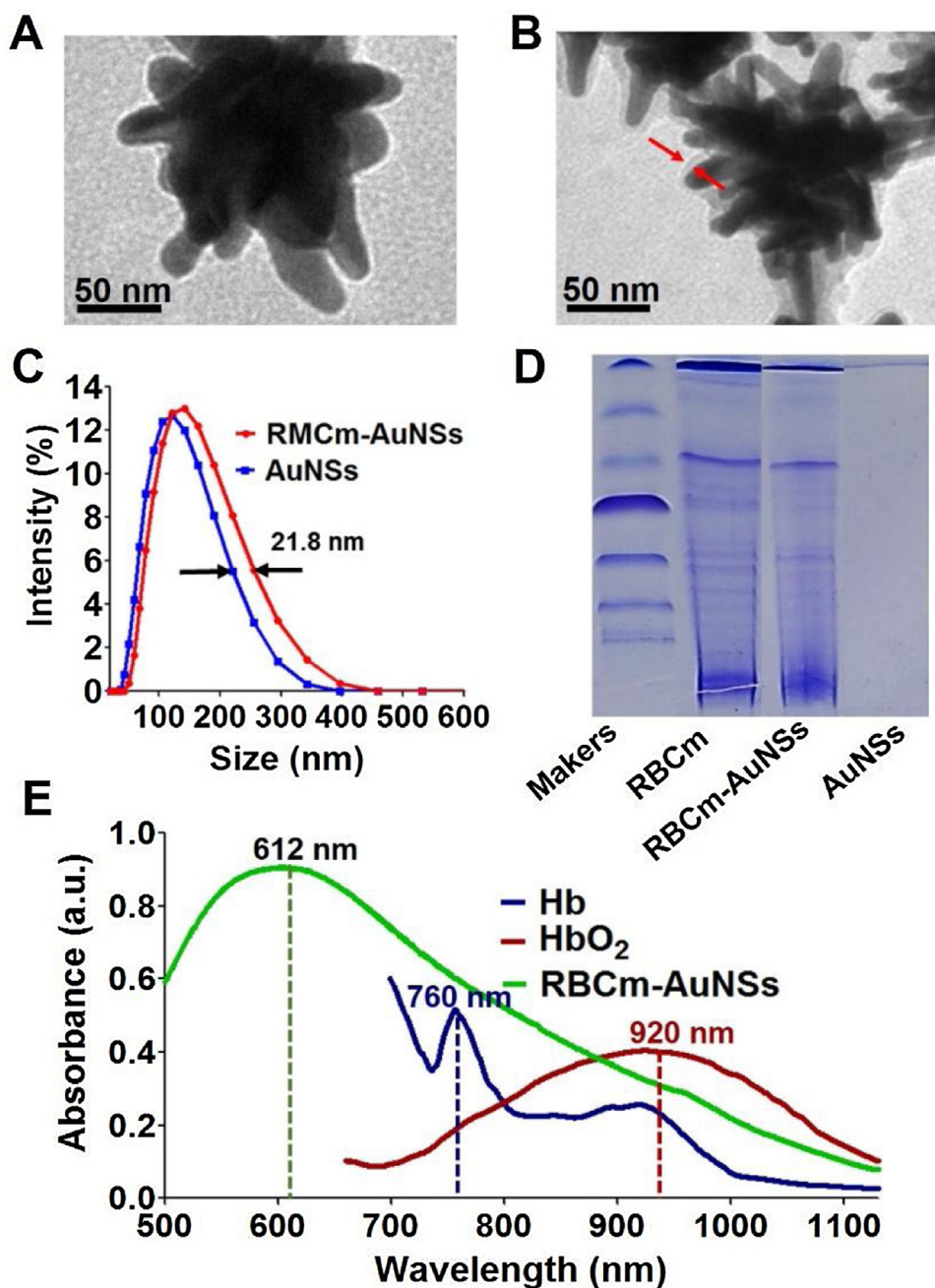
Fig. 1. Characterization of RBCm-AuNSs. TEM images for uncoated AuNSs (A) and RBCm-AuNSs (B), respectively. C. Hydrodynamic size of AuNSs and RBCm-AuNSs as measured by DLS. D. SDS-PAGE protein analysis of empty RBCs, RBCm-AuNSs, and AuNSs, respectively. E. UV–vis spectra of RBCm-AuNSs in water (100 μg/mL) and the standard absorption spectra of Hb and HbO$_2$ (obtained from MSOT).

pending RBCm-AuNSs in FBS for 3 days, the absorption peaks at 415 nm were almost unchanged (Fig. 3A), attesting to a stable structure of RBCm-AuNSs in FBS. The result suggests that RBCm-AuNSs can maintain effectiveness and performance *in vivo*. Moreover, owing to the camouflage provided by the RBC membrane extracted from mice, biomimetic RBCm-AuNSs were expected to be inherently non-toxic. To verify the hypothesis, we separately incubated two types of cells, Hep-G2 and HUH-7, with RBCm-AuNSs. As depicted in Fig. 3B, both cell lines yielded survival rates of >90% after incubation with gradient concentrations from 20 to 220 μg/mL of RBCm-AuNSs. As the concentration increased, cell activity tended to decrease slightly, probably due to the effect of osmosis. Nevertheless, both Hep-G2 and HUH-7 cell lines

displayed relatively high cell viability following the addition of RBCm-AuNSs, proving that RBCm-AuNSs do not cause major cytotoxicity.

To confirm that RBC membranes could help the nanoprobe escape the MPS clearance, intracellular uptake of AuNSs and RBCm-AuNSs was investigated in RAW264.7 phagocytes. As presented in Fig. 3C, substantially more AuNSs (Fig. 3C I and II) than RBCm-AuNSs (Fig. 3C III and IV) were trapped in RAW264.7 cells, suggesting that unclothed AuNSs are removed much more easily from the blood by the MPS. It also proves that AuNSs acquire sound capability to escape the MPS clearance after being wrapped by the erythrocyte membranes. It also should be clarified that the TEM images shown in Fig. 3C do shown considerate morphology defor-

A

B
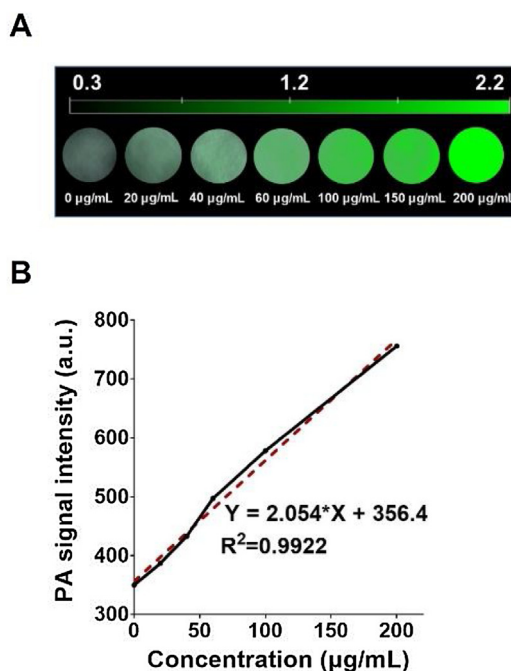
Fig. 2. A) PA images of phantom samples contains various concentrations of RBCm-AuNSs (0, 20, 40, 60, 100, 150, and 200 μg/ml). B) *in vitro* PA signal strength *versus* RBCm-AuNSs concentration.

mation to AuNS and RBCm-AuNS. Note, however, these probes are engulfed by phagocytes, being enclosed in the organelles of phagocytes; the action of intracellular forces and intracellular factors have deformed the probes [36]. In PA and PTT experiments, most RBCm-AuNS are free from the mononuclear phagocytic systems. Thus, the abovementioned morphology and optical absorption deformations will not happen.

3.4. In vivo *distribution of RBCm-AuNSs*

To explore the biodistribution of RBCm-AuNSs *in vivo*, we used traditional fluorescence imaging. The circulation time of RBCm-AuNSs in mouse blood lasted for up to 72 h, as determined by the continuous monitoring of fluorescence intensity variations at time intervals before and 1 to 72 h after intravenous administration (Fig. 4A). Note that the RBCm-AuNSs were not completely metabolized within 72 h, and the main pathway for its removal was *via* the kidney (Fig. 4B). RBCm-AuNSs quickly accumulated in the liver, with the liver-to-background ratio reaching ∼14 at 1 h (Fig. 4C). To learn more about the accumulation of RBCm-AuNSs at the tumor site, we calculated the fluorescence intensity ratio between the strongest region (presumably the tumor site) and its neighborhood. The result is shown in Fig. 4D, from which the retention of RBCm-AuNSs in the tumor is obvious: an increased concentration ratio is seen, ascribing to MPS escaping and accumulation of the clothed nanoprobes. However, due to the low resolution of traditional fluorescence imaging caused by optical scattering, we could not discern the precise boundaries and features of the tumor. After monitoring the biodistribution of RBCm-AuNSs, the mouse was necropsied, and fluorescence intensity was measured directly in the organs and tumors to study the metabolic pathways participating in RBCm-AuNS clearance. The fluorescence signal at the tumor site was ∼8×10^8, confirming the accumulation of RBCm-AuNSs in the liver tumor. This result confirmed that RBCm-AuNSs could escape elimination by the MPS and thus could accumulate at and be used to locate the liver tumors.

3.5. In vivo *photoacoustic imaging and accumulation of RBCm-AuNSs at the tumor site(s)*

In practice, the exact tumor site could be clearly detected only under dissection during fluorescence imaging. To avoid such procedure and obtain noninvasive high-resolution imaging of tumors, *in vivo* PAI experiments were performed following the protocols detailed in Section 2.11. Based on the *in vitro* photoacoustic property test for different probe concentrations (Fig. 2), we injected intravenously 200 μL of a 2 mg/mL RBCm-AuNSs solution (determined by the mouse blood volume) into mice for *in vivo* detection. In comparison, the same amount of AuNSs were injected to another group of mice. Since the laser wavelengths were chosen to distinguish the peak absorption of the nanoprobes, Hb and HbO$_2$, the PA signal strength can be directly linked with the enrichment of the unclothed and clothed probes. As we can see from Fig. 5A, with AuNSs the PA signal was strongest after 1–3 hr of injection due to the accumulation of probes in the blood. After that, the PA signal became weaker and weaker, suggesting that the unclothed probes at the moment had been mostly cleared by the MPS, even though. With RBCm-AuNSs, however, the circulation time of the probe *in vivo* was doubled and lasted for more than 72 h (Fig. 5B), which is consistent with the time duration obtained by fluorescence imaging. The prolonged circulation time is attributed to the erythrocyte membrane that helps to camouflage the nanoprobes from being cleared by the MPS. This is critical for allowing gathering of the RBCm-AuNSs at tumor sites. It also further confirms that the liver sinusoid is a blood rich environment that allows accumulation of clothed probes for the gathering of the RBCm-AuNSs at the tumor sites. More importantly, at 60 h after RBCm-AuNSs tail intravenous injection, PAI revealed three small hepatocellular carcinomas of less than 2 mm in diameter (Fig. 5B and Fig. S4), and the SNR of imaging is increased by about 55% (from 1.17 to 1.82; Fig. S5). The pathological morphological features of the tumor sites were validated by analyzing the anatomy (Fig. 5C–D) and histological analysis with H&E staining of the mouse liver (Fig. 5E). The benefits of RBCm-AuNSs escaping the MPS *in vivo* are convincing: more RBCm-AuNSs enrich in tumor result in much higher SNR of PA
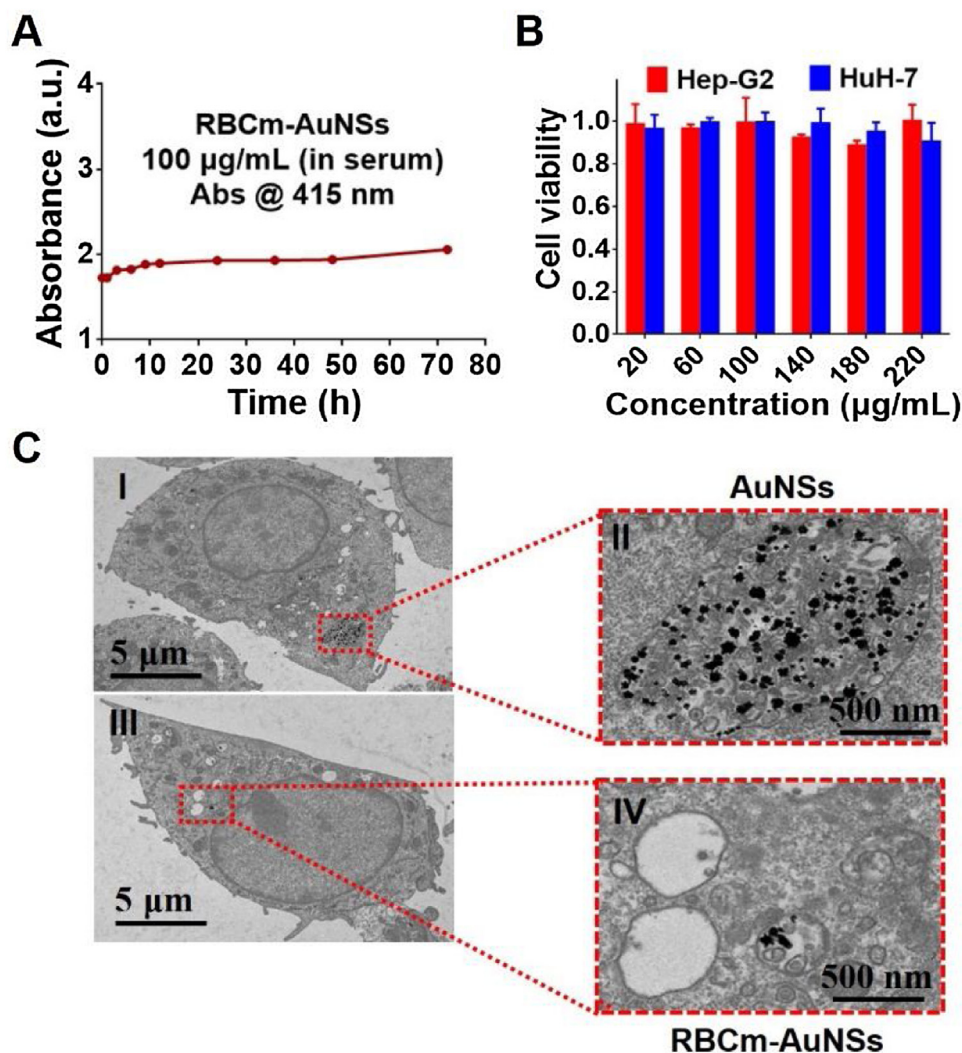
Fig. 3. A. Stability of optical absorption of RBCm-AuNSs dissolved in the serum stored under the room temperature for 3 days. Note that the observed slight increase of RBCm-AuNS absorption is probably caused by the vaporization during the course. B. Cell viability of Hep-G2 and HuH-7 cells incubated with RBCm-AuNSs of various concentrations (20, 60, 100, 140, 180, and 220 μg/mL) for 24 h, respectively. C. Cellular uptake by TEM of RAW264.7 cells cultured with AuNSs and RBCm-AuNSs, respectively, at 37 °C for 6 h. The dark spots in II and IV represent the unclothed and clothed AuNSs, respectively.

detection due to a small amount of nanoprobe discharge and prolonged circulation time. It should be noted that such an outstanding imaging capability in terms of localization, resolution, and contrast from PA imaging is not possible with fluorescence imaging. Collectively, the use of RBCm-AuNSs enables the application of PAI for the *in vivo* early diagnosis of *in situ* liver cancer.

3.6. In vitro *photothermal effect and photothermal therapy with RBCm-AuNSs*

We tested the photothermal conversion efficiency of RBCm-AuNSs after confirming their broad absorption spectrum and PA diagnosis capability. As shown in Fig. 6A, the temperature of solutions containing different concentrations of RBCm-AuNSs (20, 60, 100 μg/mL, respectively) increased substantially with exposure time, and the higher is the probe concentration, the larger is the temperature increase. In contrast, the temperature of the PBS solvent experienced small changes as it failed to absorb much NIR light energy. Thus, the observed heat accumulation was attributed primarily to the RBCm-AuNSs. In Fig. 6B, the temperature changes are quantified: the RBCm-AuNSs solutions exhibited a substantial rise in temperature, from the basal room temperature to averaged 48.0 and 62.8 °C after irradiation for 500 s at 60 and 100 μg/mL,

respectively. With identical exposure time, the photothermal effect became stronger at higher concentrations of the RBCm-AuNSs. Thus, RBCm-AuNSs could convert light energy into heat efficiently and raise the medium temperature to >45 °C, which is sufficient for the photothermal treatment of tumors. A concentration of only 60 μg/mL is required to reach the effective cell-killing temperature within 250 s. Considering the signal degeneration caused by a prolonged exposure, the photostability of RBCm-AuNSs was examined through successive exposures to NIR illumination. As shown in Fig. 6C, light irradiation and blockage modes were switched every 5 min, yet only negligible changes in the peaks and valleys were observed over the tested period, indicating good photostability of RBCm-AuNSs. Therefore, RBCm-AuNSs exhibit excellent performance of photothermal conversion ability and photostability.

The photothermal effect of RBCm-AuNSs against Hep-G2 cells was confirmed by fluorescence microscope with calcein-AM and PI staining. Calcein-AM is a cell-permeable dye that labels living cells, whereas PI is a cell-impermeable dye that only labels dead cells. Green channel images were obtained from Calcein-AM (λ excitation / λ emission, 495/515 nm), while red channel images were obtained from PI (λ excitation / λ emission, 535/617 nm). As shown in Fig. 6D, the control group (with 0 μg/mL RBCm-AuNSs) areas exhibited almost identical green fluorescence with and without
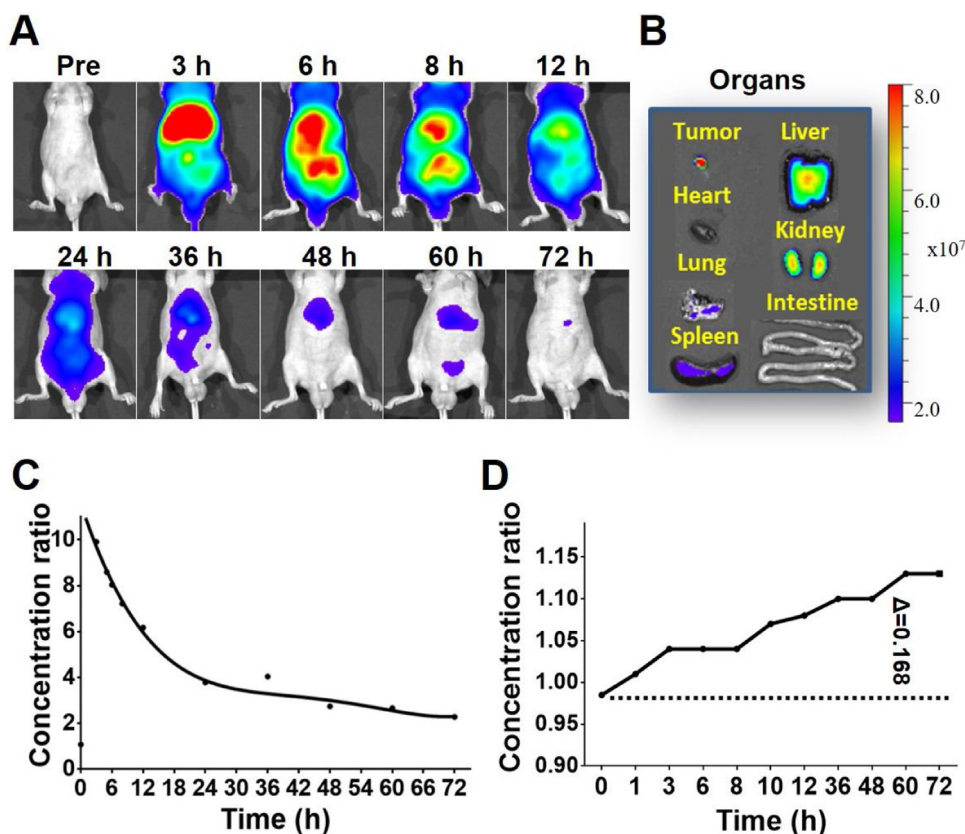
Fig. 4. *In vivo* imaging and biodistribution of RBCm-AuNSs after intravenous injection. A. The fluorescence images of Hep-G2 tumor bearing mouse at different time points. B. The fluorescence image of organs dissected from the mouse after 72 h. C. The ratio of the liver's signal value to the paw's over time. D. The signal ratio between the strongest region (presumably the tumor site) and its neighborhood over time.

laser treatment, confirming the presence of live cells. In comparison, in the 60 and 100 μg/mL RBCm-AuNSs groups, Hep-G2 cells display noticeable red fluorescence at the exposed areas, intuitively illustrating the striking photothermal effect of the RBCm-AuNSs. Notably, bright green fluorescence could be still detected at regions not exposed to laser irradiation, indicating that RBCm-AuNSs themselves did not cause tumor cell death. Moreover, the higher was the concentration of RBCm-AuNSs, the more lethal was its effect. Such an ablation capability proves that RBCm-AuNSs constitute an effective tool to eliminate cancerous cells based on the photothermal effect.

Photothermal lethality was further measured by the CCK-8 assay on different groups of cells. As reported in Fig. 6E, cell viability showed only minimal fluctuations for the different concentrations and the different treatment groups. Only in the case of cells subjected to both RBCm-AuNSs and laser exposure, viability appeared to drop drastically with the concentration increasing, and nearly all cells being counted as dead at 100 μg/mL. These results are consistent with fluorescence microscopy imaging, proving that RBCm-AuNSs or laser exposure alone have a negligible treatment effect, but their combination leads to a powerful photothermal effect against tumors.

3.7. In vivo *photothermal treatment with RBCm-AuNSs*

The accurate detection of small tumors enabled by the clothed nanoprobes and PA image could allow the treatment of liver cancer at an early stage, which is crucial to foster long-term survival. To experimentally demonstrate this possibility, the *in vivo* photothermal antitumor experiment was explored on four different groups of mice with hepatocellular carcinoma (Fig. 7). Fig. S6 shows the

temperature changes during photothermal treatment of mice in different groups. Fig. 7A presents the changes in body weight of each group of mice over time. The increase in body weight observed in the control and laser groups in the later stage may be attributed to Hep-G2 cells entering a period of exponential proliferation, which enlarged the tumors. Note that, for statistical purposes, the end time here was set to the date of all deaths in the control group (no probes or laser treatment). Mice subjected to RBCm-AuNSs treatment and laser irradiation weighted substantially more than those in the other three groups throughout the course of the experiment, suggesting that photothermal treatment was effective and that mice in this group became much healthier. Such a significant beneficial effect was also observed when comparing the survival of each group over a period of 100 days. As shown in Fig. 7B, mice from the RBCm-AuNSs with laser group exhibited the longest life span, approximately 85 days. In contrast, the RBCm-AuNSs and control groups displayed similar life spans of 40 days and the laser treatment group is 45 days. Immediately after death, the mice were dissected, and the tumors and organs were isolated. As can be seen in Fig. 7C, mice from the RBCm-AuNSs with laser group exhibited an almost complete disappearance of tumors following photothermal treatment, as indicated by the corresponding tumor weight. Combining tumor weight with body weight, revealed that the increase in the body weight observed in Fig. 7A was due to an increase in tumor proliferation, with the tumor weighting up to 3.3 g. Finally, histological analysis with H&E staining of organs in each group revealed that the RBCm-AuNSs induced no or little toxicity in healthy organs (Fig. 7D). This result again confirms the safety of the RBCm-AuNSs *in vivo*. Collectively, RBCm-AuNSs can be used as an effective tool for photothermal treatment of hepatocellular carcinoma without damage to other healthy organs *in vivo*.
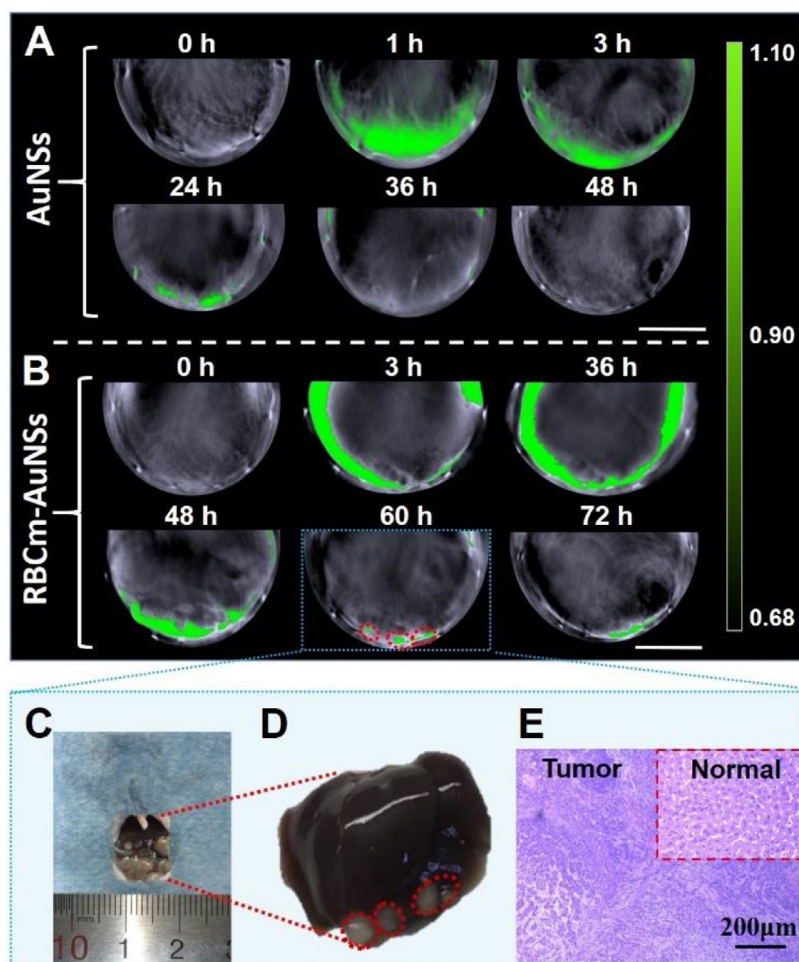
Fig. 5. *In vivo* PA images of Hep-G2 tumor-bearing mice at the liver site, before injection (0 h) and 1, 3, 24, 36, 48 h after the injection of AuNSs (A), and 3, 36, 48, 60, 72 h after the injection of RBCm-AuNSs (B). Three tumor sites were revealed from the PA imaging in RBCm-AuNSs group. Scale bars = 10 mm. C&D. The anatomy of the mouse liver after photoacoustic imaging. E. H&E staining images of tumor tissue and normal tissue of the liver.

4. Discussion

MPS clearance, one of the major challenges for the use of nanoparticles *in vivo*, restricts the enrichment of nanoparticles in the tumor and hampers the enhancement to the diagnosis and treatment of liver cancer [19,20]. The *in vivo* use of spiny nanoprobe composed of AuNSs sees no exception, although it possess excellent thermal performance and broad absorption wavelength range even in the NIR [37]. In this study, RBC membranes were applied to camouflage the AuNSs to reduce its rejection as foreign material. The results of TEM, DLS, zeta potential measurements and SDS-PAGE test demonstrated that the RBC membranes successfully clothed the spiny nanoprobes, while retaining the essential protein characteristics (Fig. 1A–D). The absorption spectrum of the clothed nanoprobes is broad and had a strong peak that can be clearly distinguished from that of oxy- and deoxy-hemoglobin (Fig. 1E). This allows for reliable extraction of PA signals contributed by the probes from a complex background such as a blood-rich environment. The result of photoacoustic property of RBCm-AuNS affirms it could be effective and excellent as a photoacoustic probe (Fig. 2).

To assess the stability and safety of RBCm-AuNSs *in vivo*, serologic stability and cytotoxicity were tested, finding sound stability (Fig. 3A) and negligible toxicity (Fig. 3B). To verify the RBCm coating can help AuNSs to avoid the immune clearance, intracellular uptake in mouse macrophage cell lines (RAW 264.7), the main component of MPS [38], was studied. The results showed that phagocytes ingested much less RBCm-AuNSs than AuNSs (Fig. 3C), indicating

RBCm-camouflaged spiny nanoprobes can evade the recognition by the MPS. Therefore, with modified nanoprobes, longer circulation in the body and stronger accumulation at the tumor sites are expected (Fig. 4). The hypothesis is that with prolonged circulation time, it is more conducive to passive targeting accumulation at the hepatic tumor due to the abundant blood in the liver sinusoid, leading to a high concentration environment of nanoprobes coated with RBCm.

Stronger immunity to the MPS clearance is also reflected from the imaging results: earlier studies [39] with AuNSs as the probe experienced substantial fluorescent signal reduction at 24 h, which is quite consistent with our photoacoustic observation (Fig. 5A). With RBCm-AuNSs, the probing window for both fluorescent and photoacoustic imaging was considerably extended to up to 72 h (Figs. 4A and 5 B). And the increase of SNR of fluorescence signal in Fig. 4D also indicates that more nanoprobes have successfully escaped the sequestration of MPS in the liver and effectively accumulated at the tumor sites. It should be pointed out that, even though fluorescence imaging can also be used for cancer imaging and diagnosis, it cannot detect or localize small liver tumors due to limited resolution at such tissue depths [40]. Hence, PAI imaging is sought for to obtain ultrasonic resolution detection of optical absorption contrast. In experiment, PAI clearly revealed three isolated *in situ* small liver tumors with dimension smaller than 2 mm in diameter under the assistant by the RBCm-AuNSs at 60 h after intravenous injection. The SNR at 60 h is 1.82, which is much higher than that with AuNSs (the number is 1.17) (Fig. S5). Such a precise
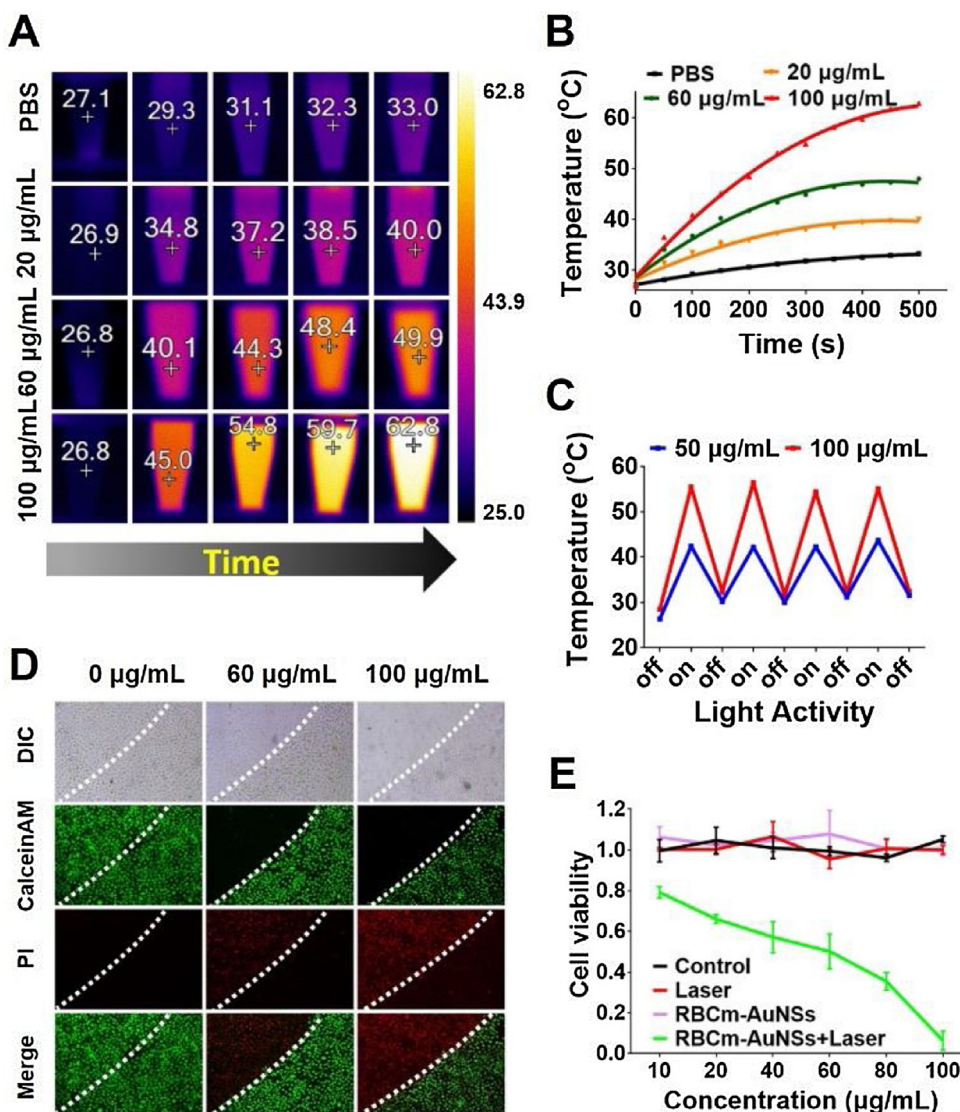
Fig. 6. A) Photothermal responses of various concentrations of RBCm-AuNSs as measured by an infrared thermal camera. B) Photothermal responses of solution suspensions with various concentrations of RBCm-AuNSs, with PBS as a reference. C) Temperature changes of RBCm-AuNSs suspensions upon five circles of NIR light irradiation-blockage gating (785 nm, 2 W/cm^2). D) CLSM images of Hep-G2 cells stained with Calcein-AM and PI after incubation with 60 and 100 μg/mL of RBCm-AuNSs and NIR laser irradiation (incubation time = 4 h, 785 nm, 2 W/cm^2, irradiation time = 300 s). E) Cell viability, representing the *in vitro* PTT efficacy, of RBCm-AuNSs of various concentrations on Hep-G2 cells upon NIR laser irradiation (Incubation time = 4 h, 785 nm, 2 W/cm^2, irradiation time = 300 s). Data was mean ± standard deviation with n = 3.

diagnosis of early-stage liver cancer allows the noninvasive irradiation of tumor sites for photothermal treatment, and the elevated concentration of clothed nanoprobes also significantly benefits the photothermal treatment outcomes: considerably more heat were generated precisely at the tumor sites and killed tumor cells efficiently (Fig. 6), resulting in healthier (Fig. 7A) and longer (Fig. 7B) life and complete disappearance of tumors (Fig. 7C). Thus, RBCm-AuNSs-assisted laser treatment was seen to substantially improve the curative prospects of *in situ* liver cancer. To this point, we have clearly demonstrated that RBCm-AuNSs could evade the MPS, prolong the circulation time *in vivo*, and increase the possibility of nanoprobe enrichment at the tumor sites, which leads to enhanced photoacoustic and photothermal effects.

5. Conclusion

To overcome the *in vivo* clearance of nanoparticles mediated by MPS, RBCm-AuNSs were designed and synthesized in this study. Following extensive characterization, the RBCm-AuNS was found to exhibit a broad and preeminent NIR absorption spectrum, to be sufficiently stable over time, and to retain the intrinsic protein characteristics of the encapsulating RBC membrane. High photothermal conversion efficiency and favorable photostability have also been proved, leading to significantly enhanced photoacoustic and photothermal capabilities. After its feasibility assessment *in vitro*, the RBCm-AuNS was used for the accurate diagnosis and treatment of mice bearing liver cancer. Assisted by the RBCm-AuNSs, photoacoustic imaging could reveal not only the existence, but also the location and dimension of tumors smaller than 2 mm in diameter. Effective photothermal treatments have also been shown in our study. Collectively, our erythrocyte membrane-camouflaged AuNSs significantly improves the biocompatibility of nanoparticles for *in vivo* use. If further advanced, the probe potentially provides a promising tool to assist the noninvasive diagnosis and treatment of early-stage cancers towards translational and clinical applications.

Declaration of Competing Interest

The authors declare no conflict of interest.
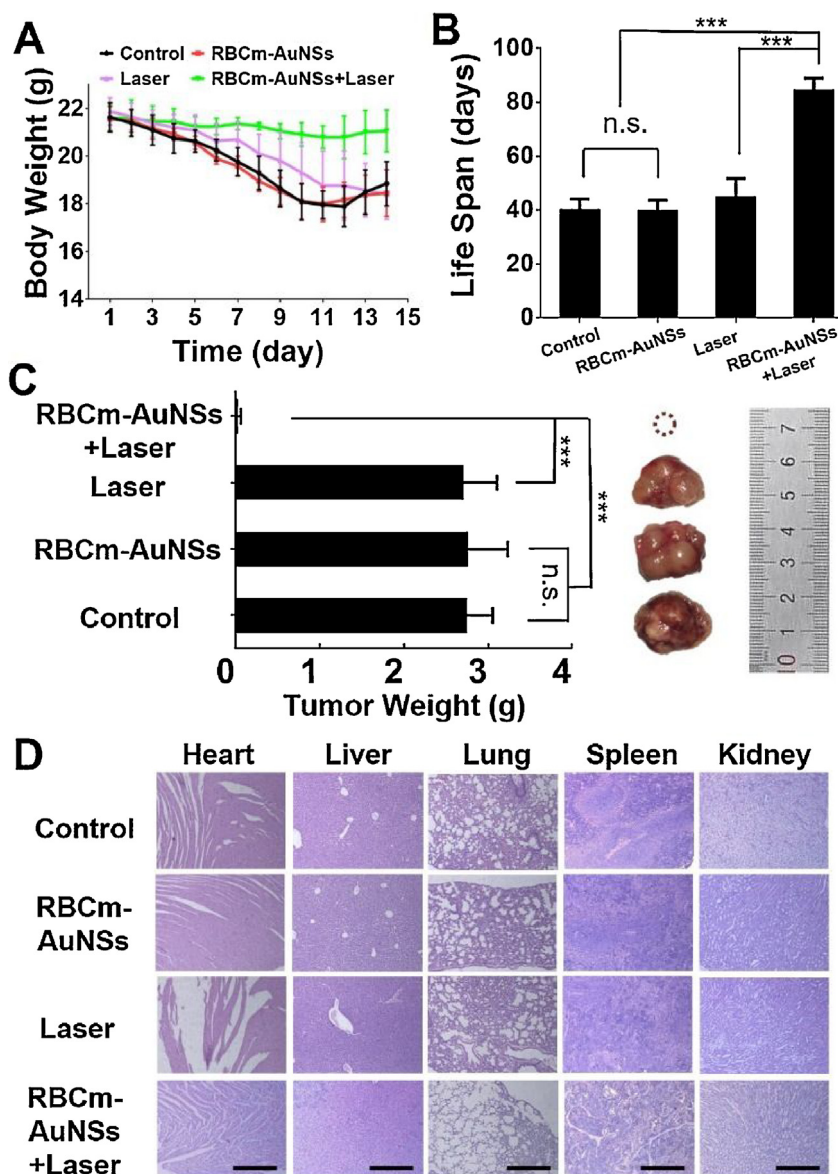
Fig. 7. *In vivo* photothermal treatment. A) Body weight of tumor bearing mice as a function of time for different groups. B) The life span of tumor bearing mice of each group. C) Tumors tissues dissected from each group after death and the comparison of tumor weight of different groups. *p < 0.01, **p < 0.001, ***p < 0.0001 and n.s. represents no significance. Data was mean ± standard deviation with n = 6. D) H&E staining images of major organs (heart, liver, spleen, lung, and kidney). Scale bars = 200 μm.

Acknowledgements

Appendix A. Supplementary data

Supplementary material related to this article can be found, in the online version, at doi:https://doi.org/10.1016/j.apmt.2019.100484.

References

[1] L.V. Wang, S. Hu, Photoacoustic tomography: in vivo imaging from organelles to organs, Science 335 (6075) (2012) 1458–1462, http://dx.doi.org/10.1126/science.1216210.

[2] F. Cao, Z. Qiu, H. Li, P. Lai, Photoacoustic imaging in oxygen detection, Appl. Sci. 7 (12) (2017), http://dx.doi.org/10.3390/app7121262.

[3] P. Lai, L. Wang, J.W. Tay, L.V. Wang, Photoacoustically guided wavefront shaping for enhanced optical focusing in scattering media, Nat. Photonics 9 (2) (2015) 126–132, http://dx.doi.org/10.1038/nphoton.2014.322.

[4] Y. Liu, H. Liu, H. Yan, Y. Liu, J. Zhang, W. Shan, P. Lai, H. Li, L. Ren, Z. Li, L. Nie, Aggregation-induced absorption enhancement for deep near-infrared II photoacoustic imaging of brain gliomas in vivo, Adv. Sci. Weinh. (Weinh.) 6 (8) (2019) 1801615, http://dx.doi.org/10.1002/advs.201801615.

[5] J. Xia, J.J. Yao, L.V. Wang, Photoacoustic tomography: principles and advances, Prog. Electromagn. Res. 147 (2014) 1–22, http://dx.doi.org/10.2528/Pier14032303.

[6] H. Deng, W. Shang, G. Lu, P. Guo, T. Ai, C. Fang, J. Tian, Targeted and multifunctional technology for identification between hepatocellular carcinoma and liver cirrhosis, ACS Appl. Mater. Interfaces 11 (16) (2019) 14526–14537, http://dx.doi.org/10.1021/acsami.8b20600.

[7] Wavefront shaping and its application to enhance photoacoustic imaging, Appl. Sci. 7 (12) (2017), http://dx.doi.org/10.3390/app7121320.

[8] F. Bray, J. Ferlay, I. Soerjomataram, R.L. Siegel, L.A. Torre, A. Jemal, Global cancer statistics 2018: GLOBOCAN estimates of incidence and mortality worldwide for 36 cancers in 185 countries, CA Cancer J. Clin. 68 (6) (2018) 394–424, http://dx.doi.org/10.3322/caac.21492.

[9] Y. Liu, P. Lai, C. Ma, X. Xu, A.A. Grabar, L.V. Wang, Optical focusing deep inside dynamic scattering media with near-infrared time-reversed ultrasonically encoded (TRUE) light, Nat. Commun. 6 (2015) 5904, http://dx.doi.org/10.1038/ncomms6904.

[10] K.H. Song, C. Kim, C.M. Cobley, Y. Xia, L.V. Wang, Near-infrared gold nanocages as a new class of tracers for photoacoustic sentinel lymph node mapping on a rat model, Nano Lett. 9 (1) (2009) 183–188, http://dx.doi.org/10.1021/nl802746w.

[11] D. Wu, L. Huang, M.S. Jiang, H. Jiang, Contrast agents for photoacoustic and thermoacoustic imaging: a review, Int. J. Mol. Sci. 15 (12) (2014) 23616–23639, http://dx.doi.org/10.3390/ijms151223616.

[12] W. Li, X. Chen, Gold nanoparticles for photoacoustic imaging, Nanomedicine (Lond.) 10 (2) (2015) 299–320, http://dx.doi.org/10.2217/nnm.14.169.

[13] V. Raghavan, C. O'Flatharta, R. Dwyer, A. Breathnach, H. Zafar, P. Dockery, A. Wheatley, I. Keogh, M. Leahy, M. Olivo, Dual plasmonic gold nanostars for photoacoustic imaging and photothermal therapy, Nanomedicine (Lond.) 12 (5) (2017) 457–471, http://dx.doi.org/10.2217/nnm-2016-0318.

[14] W. Li, X. Sun, Y. Wang, G. Niu, X. Chen, Z. Qian, L. Nie, In vivo quantitative photoacoustic microscopy of gold nanostar kinetics in mouse organs, Biomed. Opt. Express 5 (8) (2014) 2679–2685, http://dx.doi.org/10.1364/BOE.5.002679.

[15] H. Yuan, C.G. Khoury, H. Hwang, C.M. Wilson, G.A. Grant, T. Vo-Dinh, Gold nanostars: surfactant-free synthesis, 3D modelling, and two-photon photoluminescence imaging, Nanotechnology 23 (7) (2012), http://dx.doi.org/10.1088/0957-4484/23/7/075102, 075102.

[16] K. Yang, S. Zhang, G. Zhang, X. Sun, S.T. Lee, Z. Liu, Graphene in mice: ultrahigh in vivo tumor uptake and efficient photothermal therapy, Nano Lett. 10 (9) (2010) 3318–3323, http://dx.doi.org/10.1021/nl100996u.

[17] A.M. Gobin, M.H. Lee, N.J. Halas, W.D. James, R.A. Drezek, J.L. West, Near-infrared resonant nanoshells for combined optical imaging and photothermal cancer therapy, Nano Lett. 7 (7) (2007) 1929–1934, http://dx.doi.org/10.1021/nl070610y.

[18] B. Jang, L. Xu, M.S. Moorthy, W. Zhang, L. Zeng, M. Kang, M. Kwak, J. Oh, J.O. Jin, Lipopolysaccharide-coated CuS nanoparticles promoted anti-cancer and anti-metastatic effect by immuno-photothermal therapy, Oncotarget 8 (62) (2017) 105584–105595, http://dx.doi.org/10.18632/oncotarget.22331.

[19] H.H. Gustafson, D. Holt-Casper, D.W. Grainger, H. Ghandehari, Nanoparticle uptake: the phagocyte problem, Nano Today 10 (4) (2015) 487–510, http://dx.doi.org/10.1016/j.nantod.2015.06.006.

[20] K.M. Tsoi, S.A. MacParland, X.Z. Ma, V.N. Spetzler, J. Echeverri, B. Ouyang, S.M. Fadel, E.A. Sykes, N. Goldaracena, J.M. Kaths, J.B. Conneely, B.A. Alman, M. Selzner, M.A. Ostrowski, O.A. Adeyi, A. Zilman, I.D. McGilvray, W.C. Chan, Mechanism of hard-nanomaterial clearance by the liver, Nat. Mater. 15 (11) (2016) 1212–1221, http://dx.doi.org/10.1038/nmat4718.

[21] B. Li, F. Wang, L. Gui, Q. He, Y. Yao, H. Chen, The potential of biomimetic nanoparticles for tumor-targeted drug delivery, Nanomedicine (Lond.) 13 (16) (2018) 2099–2118, http://dx.doi.org/10.2217/nnm-2018-0017.

[22] X. Sun, X. Yan, O. Jacobson, W. Sun, Z. Wang, X. Tong, Y. Xia, D. Ling, X. Chen, Improved tumor uptake by optimizing liposome based RES blockade strategy, Theranostics 7 (2) (2017) 319–328, http://dx.doi.org/10.7150/thno.18078.

[23] Y. Han, R. Zhao, F. Xu, Neutrophil-based delivery systems for nanotherapeutics, Small 14 (42) (2018), e1801674, http://dx.doi.org/10.1002/smll.201801674.

[24] P. Zhang, G. Liu, X. Chen, Nanobiotechnology: cell membrane-based delivery systems, Nano Today 13 (2017) 7–9, http://dx.doi.org/10.1016/j.nantod.2016.10.008.

[25] P. Lv, X. Liu, X. Chen, C. Liu, Y. Zhang, C. Chu, J. Wang, X. Wang, X. Chen, G. Liu, Genetically engineered cell membrane nanovesicles for oncolytic adenovirus delivery: a versatile platform for cancer virotherapy, Nano Lett. 19 (5) (2019) 2993–3001, http://dx.doi.org/10.1021/acs.nanolett.9b00145.

[26] R.H. Fang, Y. Jiang, J.C. Fang, L. Zhang, Cell membrane-derived nanomaterials for biomedical applications, Biomaterials 128 (2017) 69–83, http://dx.doi.org/10.1016/j.biomaterials.2017.02.041.

[27] P.A. Oldenborg, Role of CD47 as a marker of self on red blood cells, Science 288 (5473) (2000) 2051–2054, http://dx.doi.org/10.1126/science.288.5473.2051.

[28] W. Chen, K. Zeng, H. Liu, J. Ouyang, L. Wang, Y. Liu, H. Wang, L. Deng, Y.-N. Liu, Cell membrane camouflaged hollow prussian blue nanoparticles for synergistic photothermal-/chemotherapy of cancer, Adv. Funct. Mater. 27 (11) (2017), http://dx.doi.org/10.1002/adfm.201605795.

[29] H. Ding, Y. Lv, D. Ni, J. Wang, Z. Tian, W. Wei, G. Ma, Erythrocyte membrane-coated NIR-triggered biomimetic nanovectors with programmed delivery for photodynamic therapy of cancer, Nanoscale 7 (21) (2015) 9806–9815, http://dx.doi.org/10.1039/c5nr02470f.

[30] L. Gao, H. Wang, L. Nan, T. Peng, L. Sun, J. Zhou, Y. Xiao, J. Wang, J. Sun, W. Lu, L. Zhang, Z. Yan, L. Yu, Y. Wang, Erythrocyte membrane-wrapped pH sensitive polymeric nanoparticles for non-small cell lung cancer therapy, Bioconjug. Chem. 28 (10) (2017) 2591–2598, http://dx.doi.org/10.1021/acs.bioconjchem.7b00428.

[31] L. Rao, Q.F. Meng, L.L. Bu, B. Cai, Q. Huang, Z.J. Sun, W.F. Zhang, A. Li, S.S. Guo, W. Liu, T.H. Wang, X.Z. Zhao, Erythrocyte membrane-coated upconversion nanoparticles with minimal protein adsorption for enhanced tumor imaging, ACS Appl. Mater. Interfaces 9 (3) (2017) 2159–2168, http://dx.doi.org/10.1021/acsami.6b14450.

[32] L. Rao, L.L. Bu, J.H. Xu, B. Cai, G.T. Yu, X. Yu, Z. He, Q. Huang, A. Li, S.S. Guo, W.F. Zhang, W. Liu, Z.J. Sun, H. Wang, T.H. Wang, X.Z. Zhao, Red blood cell membrane as a biomimetic nanocoating for prolonged circulation time and reduced accelerated blood clearance, Small 11 (46) (2015) 6225–6236, http://dx.doi.org/10.1002/smll.201502388.

[33] D. Dehaini, X. Wei, R.H. Fang, S. Masson, P. Angsantikul, B.T. Luk, Y. Zhang, M. Ying, Y. Jiang, A.V. Kroll, W. Gao, L. Zhang, Erythrocyte-platelet hybrid membrane coating for enhanced nanoparticle functionalization, Adv. Mater. 29 (16) (2017), http://dx.doi.org/10.1002/adma.201606209.

[34] C.M. Hu, L. Zhang, S. Aryal, C. Cheung, R.H. Fang, L. Zhang, Erythrocyte membrane-camouflaged polymeric nanoparticles as a biomimetic delivery platform, Proc. Natl. Acad. Sci. U. S. A. 108 (27) (2011) 10980–10985, http://dx.doi.org/10.1073/pnas.1106634108.

[35] Q. Cui, B. Xia, S. Mitzscherling, A. Masic, L. Li, M. Bargheer, H. Möhwald, Preparation of gold nanostars and their study in selective catalytic reactions, Colloids Surf. A Physicochem. Eng. Asp. 465 (2015) 20–25, http://dx.doi.org/10.1016/j.colsurfa.2014.10.028.

[36] N.G. Sosale, K.R. Spinler, C. Alvey, D.E. Discher, Macrophage engulfment of a cell or nanoparticle is regulated by unavoidable opsonization, a species-specific' Marker of Self' CD47, and target physical properties, Curr. Opin. Immunol. 35 (2015) 107–112, http://dx.doi.org/10.1016/j.coi.2015.06.013.

[37] Y. Wu, M.R.K. Ali, K. Chen, N. Fang, M.A. El-Sayed, Gold nanoparticles in biological optical imaging, Nano Today 24 (2019) 120–140, http://dx.doi.org/10.1016/j.nantod.2018.12.006.

[38] S. Wilhelm, A.J. Tavares, Q. Dai, S. Ohta, J. Audet, H.F. Dvorak, W.C.W. Chan, Analysis of nanoparticle delivery to tumours, Nat. Rev. Mater. 1 (5) (2016), http://dx.doi.org/10.1038/natrevmats.2016.14.

[39] H. Chen, X. Zhang, S. Dai, Y. Ma, S. Cui, S. Achilefu, Y. Gu, Multifunctional gold nanostar conjugates for tumor imaging and combined photothermal and chemo-therapy, Theranostics 3 (9) (2013) 633–649, http://dx.doi.org/10.7150/thno.6630.

[40] L.V. Wang, Multiscale photoacoustic microscopy and computed tomography, Nat. Photonics 3 (9) (2009) 503–509, http://dx.doi.org/10.1038/nphoton.2009.157.